Available online at www.sciencedirect.com
ScienceDirect
Journal of Power Sources 180 (2008) 410–422
JOURNAL OF POWER SOURCES
www.elsevier.com/locate/jpowsour

Advanced computational tools for PEM fuel cell design Part 1. Development and base case simulations

P.C. Sui [a], S. Kumar [b], N. Djilali [a,*]

[a] *Institute for Integrated Energy Systems and Department of Mechanical Engineering, University of Victoria, Victoria BC, V8W 3P6, Canada*
[b] *Ballard Power Systems, 9000 Glenlyon Parkway, Burnaby BC, V5J 5J8, Canada*

Received 18 December 2007; received in revised form 6 February 2008; accepted 6 February 2008
Available online 14 February 2008

Abstract

This paper reports on the development and numerical implementation of a comprehensive 3D computational fuel cell dynamics code for PEMFCs. The code solves a set of coupled non-linear conservation equations (mass, momentum, species, energy, electrical potential and liquid water saturation) for an entire unit cell. A phenomenological model for water transport in the membrane is solved separately for the membrane domain, in conjunction with calculation of the water content on the boundary such that that water balance is satisfied on both sides of the membrane interface, and the numerical implementation of the model is validated against an analytical solution. The global polarization curve predicted with the CFD code is found to compare favorably with reported data. A detailed validation of the CFD code against spatially resolved experimental data is presented in a companion Part 2 paper, and in this paper base case simulations for a unit cell with straight channels are presented to illustrate and analyze basic physical features, transport of species along the channel and coupling between heat and mass transfer processes. Analysis of the results shows that many of the variables of interest, including mass fractions and current densities, exhibit similar profiles along the channel, which suggests that reduced dimensional model based on appropriate similarity variables might be suitable for rapid calculations.

Keywords: Computational fluid dynamics; Modeling; Membrane transport; Water balance; Current mapping; Capillary diffusivity

1. Introduction

The last few years have seen significant developments in computational fuel cell engineering (CFCE) allowing multi-dimensional simulations of coupled transport in proton-exchange membrane fuel cells (PEMFCs), e.g. [1–9]. CFCE tools can provide invaluable assistance in analyzing thermal and water management problems in a fuel cell, in design and optimization, in guiding experimental investigations, and ultimately in improving performance and achieving cost reductions. But many challenges remain [10]. One of the hurdles in firmly establishing the reliability of CFCE tools – a prerequisite for their systematic use in real design – is the lack of validation. In principle, a numerical solution should be validated against experimental data of equal dimensions for all the variables solved in the computation. This is impractical for most fuel cells because of the limitations in existing experimental techniques and the inherent difficulties of *in situ* measurements.

State-of-the-art multi-dimensional CFCE tools are typically built on the well-established computational fluid dynamics (CFD) framework, which provides capabilities for numerical discretization and solution of coupled, non-linear convection-diffusion equations that govern a variety of thermo-fluid processes. In addition to the conventional CFD framework, the CFCE tools often involve considerations of transport processes specific to PEMFCs, including multi-phase flows in porous media and microchannels, electrochemical reactions, and transport of charged species and water in ionomer phase. Although most current commercial CFD codes can provide numerically robust and physically reliable simulations of common thermo-fluid problems, their capabilities in handling the additional complexities of a PEMFC problem still require great care to ensure robustness. Furthermore, detailed assessment and scrutiny of some of the physical models implemented in cur-

* Corresponding author. Tel.: +1 250 721 6034; fax: +1 250 721 6323.
E-mail address: ndjilali@uvic.ca (N. Djilali).

0378-7753/$ – see front matter © 2008 Elsevier B.V. All rights reserved.
doi:10.1016/j.jpowsour.2008.02.007

Nomenclature

a	water activity
$\vec{B}$	body force (N)
C_{O_2}	oxygen concentration (mol m^{-3})
$C^{l}_{O_2}$	oxygen concentration in GDL at cathode catalyst layer (mol m^{-3})
$C^{ref}_{O_2}$	cathode reference water concentration (mol m^{-3})
Cp	specific heat (J mol^{-1} K^{-1})
Cp_i	specific heat for ith species (J mol^{-1} K^{-1})
D_i	diffusion coefficient for ith species (m^2 s^{-1})
D'	diffusion coefficient (m^2 s^{-1})
D_λ	water diffusion coefficient (mol m^{-1} s^{-1})
E^0	equilibrium cell voltage
F	Faraday constant, 96487C
g	Gibbs free energy (J kg^{-1})
g_i	Gibbs free energy for species i (J kg^{-1})
h	mixture enthalpy (J kg^{-1})
h_i	enthalpy of ith species (J kg^{-1})
$\tilde{h}_i$	sensible heat of ith species (J kg^{-1})
$\vec{i}$	current density (A m^{-2})
$\vec{J}$	mass flux (kg m^{-2} s^{-1})
j_0	exchange current density (A cm^{-2})
M	molecular weight (kg mol^{-1})
M_m	equivalent weight of a dry membrane (kg mol^{-1})
$\dot{m}_i$	mass flow rate of species i (kg s^{-1})
$\dot{m}_l$	phase change rate (kg s^{-1})
N_G	number of gas-phase species
n_d	electro-osmotic drag coefficient
p	pressure (Pa)
$\vec{q}$	heat flux (W m^{-2})
R	membrane resistance (Ω)
R_u	universal gas constant (8.314 J mol^{-1} K^{-1})
RH	relative humidity
$\dot{S}_h$	enthalpy source due to phase change (W m^3)
$(S/V)_{eff}$	effective surface to volume ratio (m^2 m^3)
s	saturation
T	temperature (K)
t	time (s)
$\vec{u}$	bulk fluid velocity (m s^{-1})
V	cell voltage (V)
x	X-coordinate (between channel and land area)
y	Y-coordinate (perpendicular to MEA)
Y_i	mass fraction of ith species
z	Z-coordinate (axial)

Greek symbols

Δh^0_f	enthalpy of formation (J mol^{-1})
α	transfer coefficient
δ	average pore size (m)
ε	wet porosity
η	activation overpotential (V)
k	thermal conductivity (W m^{-1} K^{-1})
κ	permeability (m^2)
λ	water content
μ	dynamic viscosity (kg m^{-1} s^{-1})
ρ	mass density of mixture (kg m^{-3})
ρ_{dry}	density of dry membrane (kg m^{-3})
ρ_m	density of a dry membrane (kg m^{-3})
σ	electrical conductivity (S m^{-1})
τ	Bruggeman factor
τ_{pc}	phase change characteristic time (s)
$\vec{\tau}$	shear stress tensor (N m^{-2})
ϕ	electrical potential (V)
$\dot{\omega}_i$	production rate of ith species due to electrochemical reactions (kg m^{-3} s^{-1})
Λ	Species concentration (mol m^{-3})

Subscript

0	reference state
a	anode side of the membrane
b	bulk property
c	cathode side of the membrane
ch	channel
l	liquid
m	membrane property
p	pore property
rxn	reaction
s	solid

Superscript

sat	saturation

rent CFCE tools is required because these models lack either generality and/or rational foundations [10].

In this paper and its companion Part 2 [11] we report on the development of a 3D simulation code for PEMFC and its validation using spatially resolved experimental data of local current density and water mass in the MEA, with the purpose of establishing the bounds of validity of state-of-the-art CFCE methodology and identifying critical issues to improve fidelity and reliability. The paper begins with a description of the governing equations, including the phenomenological membrane model, and the coupling of these equations, followed by a description of the computational domain and boundary conditions. In Section 4, the experimental setup and post-processing of the computational results are first discussed. Detailed comparison of the numerical predictions with spatially resolved experimental data, as well as a parametric study and analysis are presented in Part 2.

2. Mathematical formulation

2.1. Governing equations

The CFCE framework combines established CFD methodology, which solves the discretized conservation equations for mass, momentum, species, and energy, with additional conservation equations needed to account for electrochemical reaction kinetics and the transport of charged species, which in gen-

eral appear as the potentials in the electrolyte phase and the electric conductor phase respectively. In addition, in a PEMFC two-phase flow and phase change of water are likely to occur, which necessitates another set of model conservation equations to describe the transport of liquid water. The multi-phase, multi-dimensional non-isothermal CFCE framework developed here is based on the following assumptions:

(1) Ideal gas for all gas species.
(2) No deformation in all parts of the cell (no swelling/shrinking of the membrane, no deformation of the GDL under the land area due to compression).
(3) Phase equilibrium of water with the electrolyte. This allows the use of membrane sorption isotherm using the water activity at the membrane boundaries.
(4) The unit cell operates at steady state.

Additional assumptions required in modeling specific transport processes in components will be discussed subsequently. A commercial CFD code, CFD-ACE+, is employed to solve the complete set of conservation equations for a unit cell geometry.

2.1.1. Conservation of mass and momentum

The volume-averaged mass and momentum conservation equations in a porous media are:

$$\frac{\partial}{\partial t}(\varepsilon\rho) + \nabla(\varepsilon\rho\vec{u}) = 0 \tag{1}$$

and

$$\frac{\partial}{\partial t}(\varepsilon\rho\vec{u}) + \nabla(\varepsilon\rho\vec{u}\vec{u}) = -\varepsilon\nabla p + \nabla(\varepsilon\vec{\tau}) + \varepsilon\vec{B} + \frac{\varepsilon^2\mu\vec{u}}{\kappa} \tag{2}$$

2.1.2. Conservation of non-charged species

The mass conservation equations for the individual gas-phase species, $i = 1, \ldots, N_G$, may be written as

$$\frac{\partial}{\partial t}(\varepsilon\rho Y_i) + \nabla(\varepsilon\rho\vec{u}Y_i) = \nabla\vec{J}_i + \dot{\omega}_i \tag{3}$$

where in general, the species diffusion flux is given by the Stefan–Maxwell equation:

$$\vec{J}_i = \rho D_i\nabla Y_i + \frac{\rho Y_i}{M}D_i\nabla M - \rho Y_i\sum_j D_j\nabla Y_j - \frac{\rho\nabla M}{M}\sum_j D_j Y_j \tag{4}$$

The effective mass diffusion coefficients of species i within the porous medium D_i is related to the porosity via the Bruggeman relation:

$$D_i = D_{i,0}\varepsilon^{\xi} \tag{5}$$

where the empirical exponent ξ is usually taken equal to 1.5. The actual values used in this work are discussed in Section 4.

2.1.3. Conservation of charged species and electrochemical reactions

Electro-neutrality dictates that the sum of all current flows equals to zero, and conservation of charged species is thus given by

$$\sum_{j=1,N_{rxn}} \nabla\vec{i}_j = 0 \tag{6}$$

In a PEMFC, charge transport consists of protonic and electronic currents, and Eq. (6) can be written as:

$$-\nabla\vec{i}_{H+} = \nabla\vec{i}_{e-} = j_T \tag{7}$$

The transfer current density is non-zero only in the region where electrochemical reactions take place. Introducing an electrical potential for each charged species and relating the potential to current density using Ohm's law, we have

$$\nabla(\sigma_m\nabla\phi_m) = -\nabla(\sigma_s\nabla\phi_s) = j_T \tag{8}$$

where ϕ_m and ϕ_s are the electric potentials of proton and electron, respectively. The transfer current, J_T, can be described under normal conditions by the Butler–Volmer equation:

$$j_{T,j} = \frac{j_{0,j}}{\prod_{k=1}^{N}[\Lambda_{k,ref}]^{\alpha_{k,j}}}\left[\exp\left(\frac{\alpha_{a,j}F}{R_uT}\eta\right) - \exp\left(-\frac{\alpha_{c,j}F}{R_uT}\eta\right)\right]\prod_{k=1}^{N}[\Lambda_k]^{\alpha_{k,j}} \tag{9}$$

where $[\Lambda_k]$ represents the average interfacial molar concentration of the kth species and the overpotential for each reaction is defined as $\eta = \phi_s - \phi_m$.

For an electrochemical reaction having the generalized form

$$\sum_{i=1}^{N_G} a'_{ij}A_i \pm e \rightarrow \sum_{i=1}^{N_G} a''_{ij}A_i \quad \text{for} \quad j = 1, 2, \ldots, N_{steps} \tag{10}$$

the transfer current density is related to gas species concentration by the so-called reaction-diffusion balance equation:

$$\sum_{j=1}^{N_{steps}} M_i(a''_{ij} - a'_{ij})\frac{j_{T,j}}{F} = \rho D_i\frac{Y_i - Y_{P,i}}{\delta} \tag{11}$$

where $Y_{p,i}$ denotes the species mass fraction in the pore-fluid, while Y_i denotes the mass fraction at the pore-fluid/catalyst interface. The mass transfer in the pore level is assumed to be limited by the diffusion from the pore to the catalyst sites, hence an average pore size is used for δ.

2.1.4. Conservation of energy

The governing equations used in the present work differ from those reported in Mazumder and Cole [5,6] mainly in the energy equation and the transport of liquid water (saturation). In [5] the energy equation is expressed and solved in terms of enthalpy, which consists of enthalpy of formation and sensible heat. In the present study, sensible heat is the primary variable for the energy equation. While combining enthalpy of formation and sensible heat in the energy equation is a common practice when dealing with reacting flows such as combustion, this formulation is not as robust for an electrochemical system involving half-cell reactions. The electrical power generated in each half-cell reaction in this formulation should appear as a sink term in

the conservation equation; however, this is not feasible because the charged species (H^+, e^-) and electrically neutral species (H_2, O_2, and H_2O) use different reference points, which makes evaluation of the Gibbs' free energy for each half-cell reaction difficult. This ambiguity can be circumvented by considering only the conservation of the sensible heat of the neutral species. All potential losses then appear as heat source terms in the energy equation, and the available electrical power is the outcome of the computation. The conservation of energy is written as:

$$\frac{\partial}{\partial t}((1-\varepsilon)\rho_S h_S + \varepsilon\rho h) + \nabla\cdot(\varepsilon\rho\vec{u}h) = \nabla\cdot\vec{q} + \varepsilon\vec{\tau}:\nabla\vec{u} + \varepsilon\frac{\mathrm{d}p}{\mathrm{d}t} + j_T\left(\frac{S}{V}\right)_{\text{eff}}\eta + \frac{\left|\vec{i}\cdot\vec{i}\right|}{\sigma} + \dot{S}_h \quad (12)$$

where

$$\vec{q} = \lambda\nabla T + \sum_{i=1}^{N_G}\vec{J}_i(h_i - g_i) \quad (13)$$

The quantity $\sum_{i=1}^{N_G}\vec{J}_i g_i - j_T(S/V)_{\text{eff}}\eta$ is the electrical work done during an electrochemical reaction. Note that

$$\sum_{i=1}^{N_G}\vec{J}_i(h_i - g_i) + j_T\left(\frac{S}{V}\right)_{\text{eff}}\eta = \sum_{i=1}^{N_G}\vec{J}_i T s_i + j_T\left(\frac{S}{V}\right)_{\text{eff}}\eta \quad (14)$$

where the first term on the right hand side represents reversible heat generation and the second term represents irreversible heat generation. These losses are in addition to the Joule heating term, which also causes irreversible heat generation in the cell.

2.1.5. Transport of liquid water

The transport of liquid water is described in terms of conservation of liquid saturation, taking into account evaporation/condensation, capillary diffusion and gravity:

$$\frac{\partial}{\partial t}(\varepsilon_d\rho_l s) + \nabla(\varepsilon_d\rho\vec{u}s) = \nabla(\varepsilon_d\rho_l D_c\nabla s) - \nabla\left(\frac{s(1-s)\kappa(\rho_l-\rho_g)}{\nu}\vec{g}\right) + \dot{m}_l \quad (15)$$

The evaporation/condensation rate is expressed as:

$$\dot{m}_l = \begin{cases} \varepsilon_d\rho(Y^{\text{sat}}_{H_2O} - Y_{H_2O})/\tau_{pc} \\ 0; \quad \text{if } s \le 0 \text{ and } \dot{m}_l > 0 \end{cases} \quad (16)$$

Eq. (15) is applied for flows in porous media as well as ordinary fluid flow for liquid water saturation, even though in the ordinary fluid phase, liquid saturation loses its physical meaning as volume fraction of liquid water in the pore. The capillary pressure formulation used in [6] is adopted with a slight modification in the rate of phase change.

2.2. Membrane model

In Mazumder and Cole [5] the transport of non-vapor water is modeled as liquid, and water movement due to the electro-osmotic drag (EOD) is included as a convective term in the conservation equation for liquid water. One drawback with this approach is that it fails to account for water transport inside the membrane phase when the vapor phase is at undersaturated conditions. In the present study, a separate model for water transport in the membrane phase is adopted. The phenomenological model describes the water movement due to the EOD and diffusion and is solved only for the membrane part of the unit cell. The implementation of this model within the CFD framework requires special treatment for mass transfer on the membrane–catalyst layer interface to ensure continuity of water species.

The mechanisms for transport of water in the electrolyte phase differ from those in vapor phase. The dominant water

Table 1
Conservation equations solved in the comprehensive numerical simulation

	Convection	Diffusion	Source
Mass	$\nabla(\varepsilon\rho\vec{u})$	–	$\dot{m}$
Momentum	$\nabla(\varepsilon\rho\vec{u}\vec{u})$	$-\nabla P + \nabla(\varepsilon\bar{\tau})$	$-\left(\varepsilon^2\frac{\mu}{k_p}\right)\vec{u}$
Energy	$\varepsilon C_p\rho\vec{u}\nabla(T)$	$\nabla(\lambda\nabla T) + \sum_i J_i c_{p,i}\nabla T$	$\left[j_T\eta + \sum_{i=1}^{N_G}\vec{j}_i(h_i-g_i)\right]\left(\frac{S}{V}\right)_{\text{eff}} + \frac{\left\vert\vec{i}\vec{i}\right\vert}{\sigma} + \dot{S}_h + \dot{Q}$
Species	$\nabla(\varepsilon\rho\vec{u}Y_i)$	$\nabla\vec{J}_i$[a]	$\rho D_i\frac{Y_i - Y_{P,i}}{\delta}\left(\frac{S}{V}\right)_{\text{eff}}$
Potential	–	$\nabla(\sigma_k\nabla\Phi_k)$	$j_{0,k}\left(\frac{c_k}{c_{k,\text{ref}}}\right)^{\gamma_k}(e^{\alpha_{a,k}f\eta} - e^{-\alpha_{c,k}f\eta})\left(\frac{S}{V}\right)_{\text{eff}}$
Saturation	$\nabla(\varepsilon_d\rho_l\vec{u}s)$	$\nabla[\varepsilon_d\rho_l D_c\nabla s]$	$\varepsilon_d\frac{\rho}{\tau}\left(\frac{m_w p_{\text{sat}}}{mP} - Y_w\right)$[b]
Water content	$\nabla\left(\frac{n_d}{F}\vec{i}\right)$	$-\frac{\rho_m}{M_m}\nabla(D_\lambda\nabla\lambda)$	–

[a] $\vec{J}_i = \rho D_i\nabla Y_i + \frac{\rho Y_i}{M}D_i\nabla M - \rho Y_i\sum_j D_j\nabla Y_j - \frac{\rho Y_i\Delta M}{M}\sum_j D_j Y_j$.

[b] $V = \max(U_d, U)$, $U_d = \frac{D_w}{L}$, $L = \left[\frac{\sum_{ic}^{Nc} C\,\text{vol}(ic)}{Nc}\right]^{1/3}$.

transport mechanisms in the membrane include the EOD associated with the movement of charged species, diffusion driven by gradient of chemical potential, and hydraulic permeation due to pressure gradients. In the present work, the contribution due to pressure gradient is assumed negligible based on experimental observation that the membrane permeability is extremely low for gas and liquid. The flux of water inside the membrane is replaced by the net water flux given by a phenomenological model of a form similar to Eq. (4), consisting of an EOD term and a diffusion term. The flux, expressed in terms of *water content* λ (number of water molecules absorbed per sulphonic acid site), is thus given as:

$$\vec{J}_\lambda = \frac{n_d}{F} i - \frac{\rho_{dry}}{M_m} D_\lambda \nabla \lambda \tag{17}$$

Both the drag coefficient and water diffusion coefficient are functions of water content and temperature:

$$n_d = n_d(\lambda, T), \tag{18}$$

and

$$D_\lambda = D_\lambda(\lambda, T) \tag{19}$$

In the present study the water transport in the membrane is solved separately from the gas species equation. On the membrane boundaries, the flux of water calculated using (17) enters the catalyst layer domain, while the water content boundary condition on the membrane boundaries is obtained through an adsorption isotherm for water in the electrolyte phase. The adsorption isotherm is a phase equilibrium condition that relates the water content to water activity and temperature in the vapor phase on the membrane boundary:

$$\lambda = \lambda(a, T) \tag{20}$$

where the water activity (a) corresponds to the relative humidity of water vapor. The ionic conductivity of the electrolyte is generally considered a function of water content and temperature:

$$\sigma = \sigma(\lambda, T) \tag{21}$$

Substituting for the water flux in Eq. (3) with Eq. (17) and using transport properties of Eqs. (18), (19) and (21), and the phase equilibrium relationship of (20), the transport of water in the membrane is solved and coupled iteratively with the domain outside of the membrane. Numerical analysis and behavior of this formulation is discussed in Sui and Djilali [12] and Mazumder [13]. The properties reported by Springer et al. [14], cf. Appendix B, are used for the calculation unless otherwise noted. More details regarding the phenomenological model can be found in Janssen [15], and a critical examination and analysis of the transport models for polymer membranes is given in Fimrite et al. [16].

2.2.1. Anisotropic transport properties for solid and porous media

Most of the components of a PEMFC have anisotropic transport properties. The gas diffusion layer (GDL) in particular shows significant differences in the transport of electricity and heat in the in-plane and the through-plane directions. The catalyst layer is a composite material that is constructed by two networks (electrolyte and carbon black respectively), which shows some degree of anisotropy due to fabrication processes and also possibly due to preferred material orientation. The bipolar plate that is made of graphite powder and resin binder has some flaky structure that makes its transport properties anisotropic. Among all these materials, the anisotropy in the GDL is believed to be the most influential because of its fibrous structure as well as the fact that it is subject to discontinuous property change on one boundary, i.e. on the side that is in contact with the bipolar plate [17]. Furthermore, part of the GDL on the GDL-bipolar plate interface is under compression and the transport through such regions is complicated [18,19]. Owing to the complexity of coupled transport phenomena, analysis on the effects due to anisotropy in transport properties of the materials in a PEMFC is best assisted by employing a simulation tool.

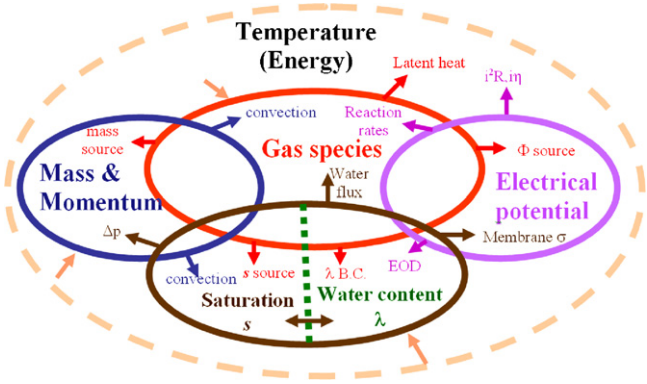

Fig. 1. Coupling of conservation equations in PEMFC simulation.

The transport property for a thermal or electrical conduction equation takes the form of a tensor:

$$\vec{k} \equiv \begin{vmatrix} k_{xx} & k_{xy} & k_{xz} \\ k_{yx} & k_{yy} & k_{yz} \\ k_{zx} & k_{zy} & k_{zz} \end{vmatrix} \tag{22}$$

For a conventional plate-and-frame type of membrane electrode assembly (MEA) with coordinates X and Z as the in-plane direction and Y as the through-plane direction, we assume the transport is limited in both planes, i.e. only diagonal terms in the matrix remain. For a PEMFC problem, the anisotropy should appear in the conservation of species (diffusivity), momentum (permeability), energy (heat conductivity) and potential (electrical conductivity).

2.3. Coupling of transport equations

Table 1 summarizes the governing equations implemented and solved in the CFD code. One of the most challenging aspects from a computational view point is the coupling between the various transport phenomena within a PEMFC as illustrated in Fig. 1. Each circle represents a conservation equation and the outward-pointing arrows represent the effects of the conservation equation in question on other equations. The conservation

equation of gas species, water in liquid and solid (membrane) phases, and energy are closely coupled with all other conservation equations. Among all the processes considered, the transport of water, which exists in the system in the forms of vapor, liquid, and absorbed in solid, is central to all other coupled transport processes. Unsaturated water in the vapor phase affects local relative humidity near the membrane, especially on the anode side, and thus affects water transport across the membrane as well as electrical properties of the membrane, which in turn impacts the solution for the electric potential. The transport of liquid water in the porous media affects mass transport of gas species, while liquid water in the gas channels changes the pressure field and may alter flow distribution in a unit cell. Transport of water across the membrane is a key phenomenon that links the transport processes between the anode and cathode sides. Therefore modeling of water transport in the membrane phase is crucial to the simulation capability development for PEMFC.

The electrical potential plays two roles in the coupling. On the one hand it can be considered as representing conservation of charged species (protons and electrons), and on the other hand it can be viewed as part of the conservation of energy, in which the electrical power converted from the electrochemical reaction manifests in a potential. The electrical potentials are conveniently solved separately from the species equations to avoid the implicitness of the potential difference that appears in the Butler–Volmer equation used for the reaction rate in the gas species equations. This effectively decouples the two half-cell reactions in the anode and cathode, and as a result convergence in the gas species is not as robust as that in the conventional treatment of chemical reactions in CFD. While it is possible to include the potential into the energy equation, the difficulty is that the chemical energy and the electrical energy have different reference points.

3. Numerical implementation

To ensure continuity of water transfer across the membrane–catalyst layer interface, the water content value on this interface is calculated by

$$-\rho D\frac{Y_c - Y_w}{\delta_c} = \frac{n_d(\lambda_w)i_w}{F} - \rho_m D_\lambda(\lambda_c)\frac{\lambda_w - \lambda_m}{\delta_m} \quad (23)$$

Fig. 2 shows the relation of the variables in Eq. (17) in the vicinity of the membrane boundary. The proper implementation of the membrane model into CFD-ACE was checked against a 1D solver for Eq. (1), cf. Sui and Djilali [12], with prescribed current density and boundary condition values on the membrane, see Fig. 3. The predicted polarization curve obtained using the code with the membrane water transport model as well as the curve predicted with the code described in Mazumder and Cole [5] are compared to the experimental data of Ticianelli et al. [20] in Fig. 4, showing a clear improvement in the predictions with the implementation of the membrane water transport model. These predictions were made by setting all model parameters to correspond to those given in [20].

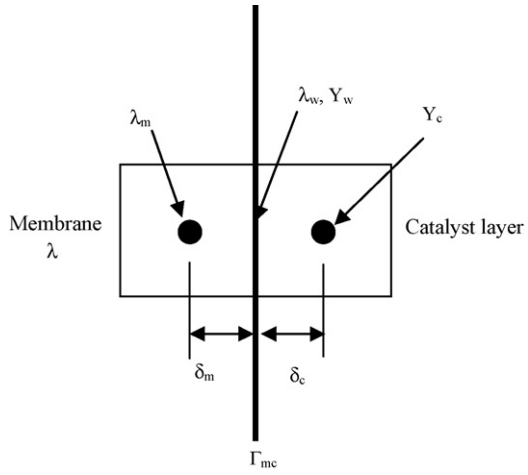

Fig. 2. Boundary condition on the membrane/catalyst layer interface.

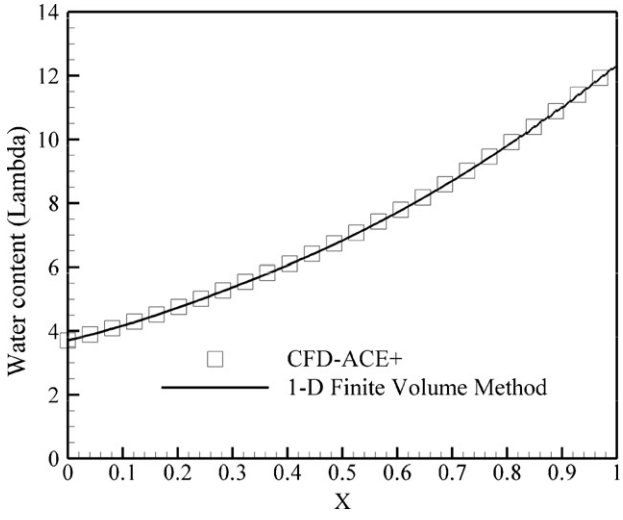

Fig. 3. Numerical validation of the membrane model implemented in the simulation.

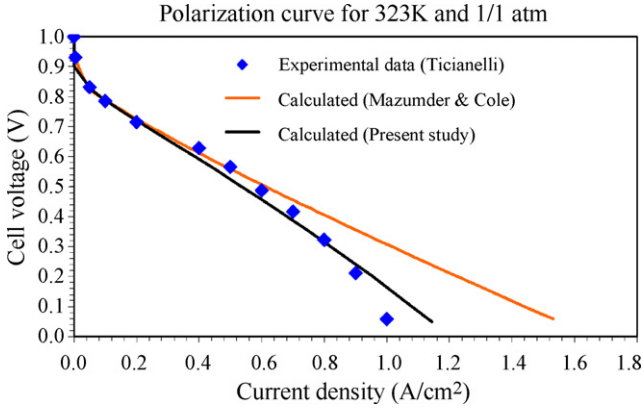

Fig. 4. Comparison of polarization curves by experiment and 2D predictions with and w/o Springer model for membrane. Springer model apparently predicts the current more close to measurement because the water transport across the membrane is better accounted for.

Table 2
Summary of properties and parameters used for the baseline calculation

	Unit	Bipolar plate	Anode gas channel	Anode GDL	Anode catalyst layer	Membrane	Cathode Catalyst layer	Cathode GDL	Cathode gas channel	Coolant channel
Dimension	m	–	2.5×10^{-4}[a]	2×10^{-4}	3.5×10^{-5}	5.4×10^{-5}	3.5×10^{-5}	2.4×10^{-4}	3.9×10^{-5}[a]	3.5×10^{-5}[a]
Porosity		–	–	0.6	0.6	0.1	0.6	0.6	–	–
Average pore size	m	–	–	2.5×10^{-6}	1×10^{-7}	1×10^{-9}	1×10^{-7}	2.5×10^{-6}	–	–
Bruggeman ξ		–	–	1	2	13	2	1	–	–
Permeability	m^2	–	–	1×10^{-13}	1×10^{-13}	1×10^{-21}	1×10^{-13}	1×10^{-13}		
Thermal conductivity	$W\,m^{-1}\,K^{-1}$		–	20	20	20	20	20	–	–
Electrical conductivity	$(\Omega\,m)^{-1}$		–	200	80	–	80	200	–	–
Protonic conductivity	$(\Omega\,m)^{-1}$	–	–	–	5	Springer	5	–	–	–
Diffusion coefficient	$m^2\,s^{-1}$	–	$Sc = 0.7$	$Sc = 0.7$	$Sc = 0.7$	Springer	$Sc = 0.7$	$Sc = 0.7$	$Sc = 0.7$	–
Density	$kg\,m^{-3}$	1600	IG	IG	IG	1980	IG	IG	IG	
Viscosity	$kg\,m^{-1}\,s^{-1}$	–	MKT	MKT	MKT	–	MKT	MKT	MKT	
Reaction		–	–	–	HOR	–	ORR	–	–	–
Coefficients for reaction	$j_0 = A\,m^{-3}$, $S/V = m^{-1}$	–	–	–	$\alpha_a = 0.5$, $\alpha_c = 0.5$, $j_0 = 1 \times 10^{-9}$, $\gamma_{H_2} = 1$, $S/V = 1000$	–	$\alpha_a = 1$, $\alpha_c = 1.2$, $j_0 = 5 \times 10^{-6}$, $\gamma_{O_2} = 1$, $S/V = 1000$	–	–	–

IG, ideal gas [21]; MKT, mixed kinetic theory [21]; HOR, hydrogen oxidation reaction; ORR, oxygen reduction reaction; *Sc*, Schmidt number. Unless otherwise stated, all other data obtained from [25].
[a] Hydraulic diameter.

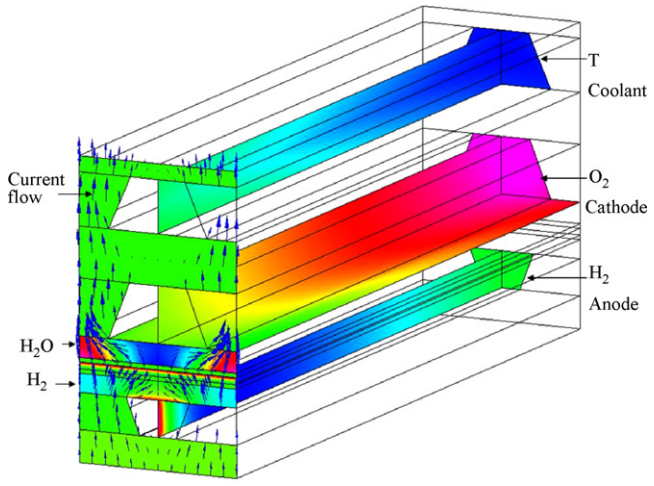

Fig. 5. Computational results of the baseline case.

3.1. Computational domain and boundary conditions

The generic computational model was applied to simulate a straight channel unit cell configuration related but not identical to the Ballard Mk902 hardware, cf. Fig. 5. Properly designed and optimized, such straight channel configurations can offer a good balance between various thermo-fluid and manufacturing requirements, and are becoming more common in industrial stacks. The computational model corresponds to the experimental cell which consists of an array of evenly spaced straight channels with a length of 0.6 m. The computational domain includes the segment bounded by the center lines of two consecutive land areas with the full length of the unit cell, which includes the MEA, gas and coolant channels, all surrounded by the bipolar material. All cases reported are with anode and cathode gases flowing in opposite directions ('counter-flow') and coolant flowing in the same direction as the cathode flow. An adiabatic boundary condition is applied to all surfaces of the computational domain except for the openings of the flow channels, which have prescribed temperature conditions.

3.2. Post-processing of 3D data

The experimental data provides spatial resolution *along* the channel direction but the distributions are essentially averaged in the spanwise direction. In order to allow direct comparison, the 3D computational results are integrated in the appropriate dimensions. For the channel flows, the flow quantities are integrated at each location over the channel cross-section using the following equations:

Mass flow rate:

$$\dot{m}_i(z) = \int \rho u Y_i \, \mathrm{d}A_{\mathrm{ch}}, \tag{24}$$

Liquid water in gas channel:

$$\dot{m}_{\mathrm{w}}(z) = \int \rho_{\mathrm{w}} u s \, \mathrm{d}A_{\mathrm{ch}}, \tag{25}$$

Bulk fluid temperature:

$$T_{\mathrm{b}}(z) = \frac{\int \rho u C p T \, \mathrm{d}A_{\mathrm{ch}}}{\int \rho u C p \, \mathrm{d}A_{\mathrm{ch}}}. \tag{26}$$

The water balance is calculated using the inlet and outlet values of water mass flow rates:

$$\alpha \equiv \frac{(\dot{m}_{\mathrm{H_2O,OUT}} - \dot{m}_{\mathrm{H_2O,IN}})_{\mathrm{anode}}}{\dot{m}_{\mathrm{H_2O,generated}}}$$

$$= \frac{(\dot{m}_{\mathrm{H_2O,OUT}} - \dot{m}_{\mathrm{H_2O,IN}})_{\mathrm{anode}}}{(\dot{m}_{\mathrm{O_2,IN}} - \dot{m}_{\mathrm{O_2,OUT}}) 2 M_{\mathrm{H_2O}} / M_{\mathrm{O_2}}} \tag{27}$$

The average current density is calculated on the outer surface of the cathode current collector:

$$I(z) = \frac{\int i \, \mathrm{d}A_{\mathrm{cc}}}{A_{\mathrm{cc}}} \tag{28}$$

Membrane resistance:

$$R(z) = \frac{\int \int \left(\frac{1}{\sigma} \mathrm{d}y\right) \mathrm{d}A_{\mathrm{cc}}}{A_{\mathrm{cc}}} \tag{29}$$

The water weight per puck is calculated by adding the water in the electrolyte phase and liquid water in the pore:

$$m_{\mathrm{H_2O},j}(\mathrm{chop}) = \int \rho_\lambda \varepsilon_{\mathrm{ionomer}} \lambda \, \mathrm{d}V_j + r_j s \rho_{\mathrm{H_2O}},$$

$$j = \mathrm{GDL, CL, PEM} \tag{30}$$

4. Results and discussion

4.1. Parameter and properties used for the baseline case

Table 2 lists the parameter values and properties used for the baseline calculations. The calculation method of standard transport properties (density, diffusion coefficient, viscosity, thermal conductivity) for gas species are given in [21]. The permeability and porosity and the Bruggeman coefficient for the membrane are chosen to effectively preclude permeation across the membrane due to a pressure difference across the membrane. The electrical conductivity of the GDL is isotropic for the baseline case but calculations using anisotropic conductivities are possible. The protonic conductivity of the electrolyte phase in the catalyst layers is set to a constant for the baseline for simplicity. The transfer coefficient for oxygen reduction reaction (ORR), α_{c}, is the only control parameter anchored to fit the polarization data. Once anchored at a particular condition, the same value is used to generate the performance curve.

4.2. Baseline conditions

Fig. 5 shows some computational results of the baseline case. In the 3D model, one can see gradient in species mass fraction and current flow in the direction between the channel area and the land area. Although these gradients may have significant impact on cell performance and durability, such gradients are not the

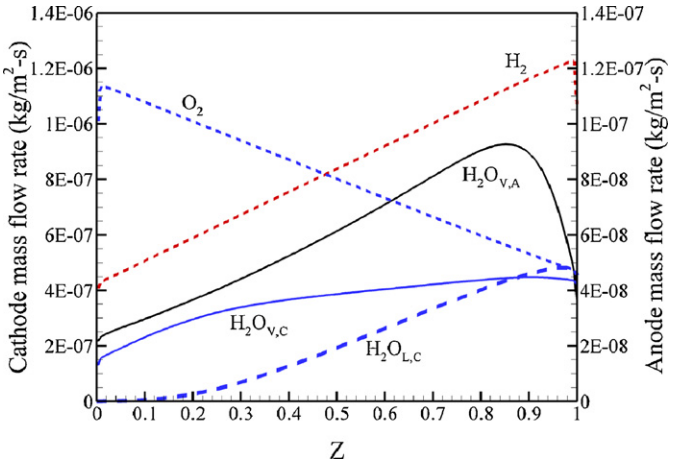

Fig. 6. Mass flow rate of gas and liquid in the gas channels.

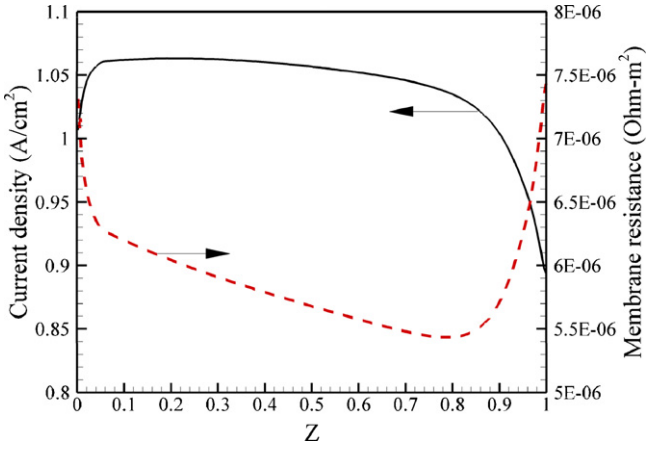

Fig. 8. Current density and membrane resistance.

focus of the present study; readers are referred to the recent work of Freunberger et al. [22] for a discussion of this issue. In the present study, we focus on validation based on the gradients in the axial direction (along the channel) to coincide with the available experimental data. Figs. 6–9 show the computational results of the baseline case plotted in the axial direction of the unit cell with the cathode inlet (anode outlet) located $Z=0$ and the cathode outlet (anode inlet) at $Z=1$. The transport properties and dimensions used in the computation are summarized in Table 2. Operating conditions of the unit cell for the baseline case are: $I=1\,\mathrm{A\,cm^{-2}}$; $P=3$ bars, RH = 55%, inlet temperature = 65.1 °C, and stoichiometric ratio = 1.71 for the cathode; and $P=3.2$ bars, RH = 19%, inlet temperature = 73.9 °C, and stoichiometric ratio = 1.54 for the anode. Fig. 6 shows the mass flow rates of gas species and liquid water along the channel calculated using Eqs. (24) and (25), respectively. It should be noted that the mass flow rates in the anode channel (right vertical axis in Fig. 6) are roughly an order of magnitude less than in the cathode side (left axis in Fig. 6). The fuel and oxidant flow rates appear to decrease almost linearly along the channel, which indicates the local flow rate into the GDL/channel interface is nearly constant at any location of the channel. However this flow redistributes inside the MEA by diffusion based on local potential distribution under the land area. The local consumption rates of the oxidant and the fuel thus become less closely related to local current density distribution. The common assumption made for along-the-channel type of models, see e.g. [23,24], whereby local reactant consumption is related to local current density is therefore not valid. The water vapor in the anode channel shows an increase near the inlet portion followed by a decrease downstream. The increase of water vapor flow close to the inlet is mainly due to back diffusion from the cathode outlet, which is likely fully humidified. As the anode channel is gradually humidified, the EOD begins to take effect and drags increasingly more water into the cathode side; thus a pattern of net water recirculation forms within the unit cell. The water vapor flow rate in the cathode first increases slightly near the inlet, and then stabilizes as the cathode stream becomes fully saturated. Liquid water only appears in the cathode channel for

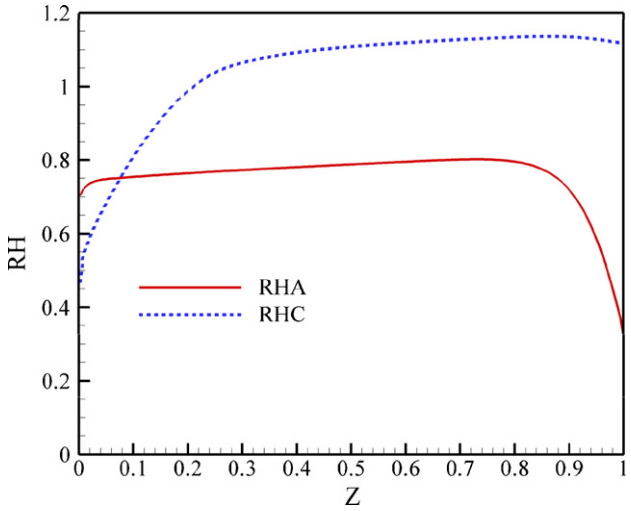

Fig. 7. Relative humidity in the gas channels.

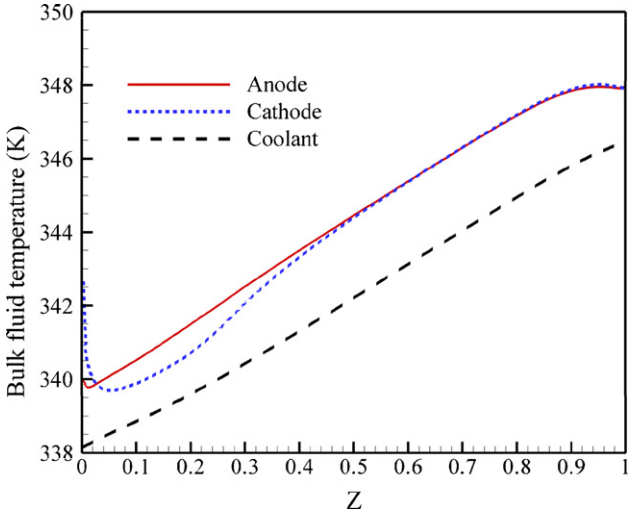

Fig. 9. Temperature profiles in the gas channels.

the baseline case. As the cathode flow proceeds downstream, it takes up more product water from the ORR, but near the cathode outlet a slight decrease in the liquid flow rate is observed due to back diffusion of water through the membrane to the anode. Fig. 7 shows the RH calculated based on bulk fluid temperature and vapor flow rate in the anode and cathode channels. The water diffusion across the membrane is primarily dependent on the water activities on both sides of the membrane, which is closely related to the RH in the channels. When RHA > RHC (approximately $Z < 0.1$ in Fig. 7), diffusion of water in the membrane is in the same direction of the EOD, while in the rest of the unit cell, water diffusion opposes water transport via the EOD. Near the anode inlet, where the difference in RH between anode and cathode is largest, back diffusion from the cathode side dominates water transport across the membrane and the net transport of water is from cathode to anode.

Fig. 8 shows the current density profile and membrane resistance along the flow channels. Two higher resistance regions can be observed near the anode and cathode inlets respectively as a result of the low RH values in these regions. The higher resistance causes a small current fall off near the cathode inlet and a larger drop near the anode inlet, where the high resistance is compounded by lower oxygen concentration on the cathode side. Fig. 9 shows the bulk fluid temperature profiles for the reactant and coolant channels. One can see that the coolant temperature varies almost linearly along the coolant channel, with a temperature increase of about 8 °C. It should be noted that in general serpentine flow channel cells would be expected to exhibit lower temperature differences due the lower geometric aspect ratio and enhanced heat transfer due to the inherent cross and counter flow feature of serpentine arrangements.

4.3. Similarity of computational results

The straight channel unit cell geometry considered here enables not only less ambiguous profile measurement for comparison with numerical results, but is also convenient for assessing the validity of simplified models with reduced dimension. Since the length scale of the cell along the flow is much larger than all other dimensions, the gradients in the axial direction are expected to be relatively smaller. This suggests that locally the solutions of all variables are dictated by the 2D cross-section perpendicular to the axial direction. Fig. 10 shows the profiles of oxygen and water mass fraction as well as current density on the GDL/catalyst layer interface at ten evenly spaced axial locations. For each variable shown in Fig. 10, these profiles can be collapsed into one profile by normalizing the local profile with the difference between the maximum and the minimum value of the profile, cf. Fig. 11.

The profile similarity suggests that a 2D computational domain may be suitable for obtaining a base solution for the coupled transport, and with appropriate scaling of the base solution, approximate solutions can be obtained for a 3D geometry. This approach would considerably reduce computational resource requirements and is attractive in the context of systematic parametric studies and optimization.

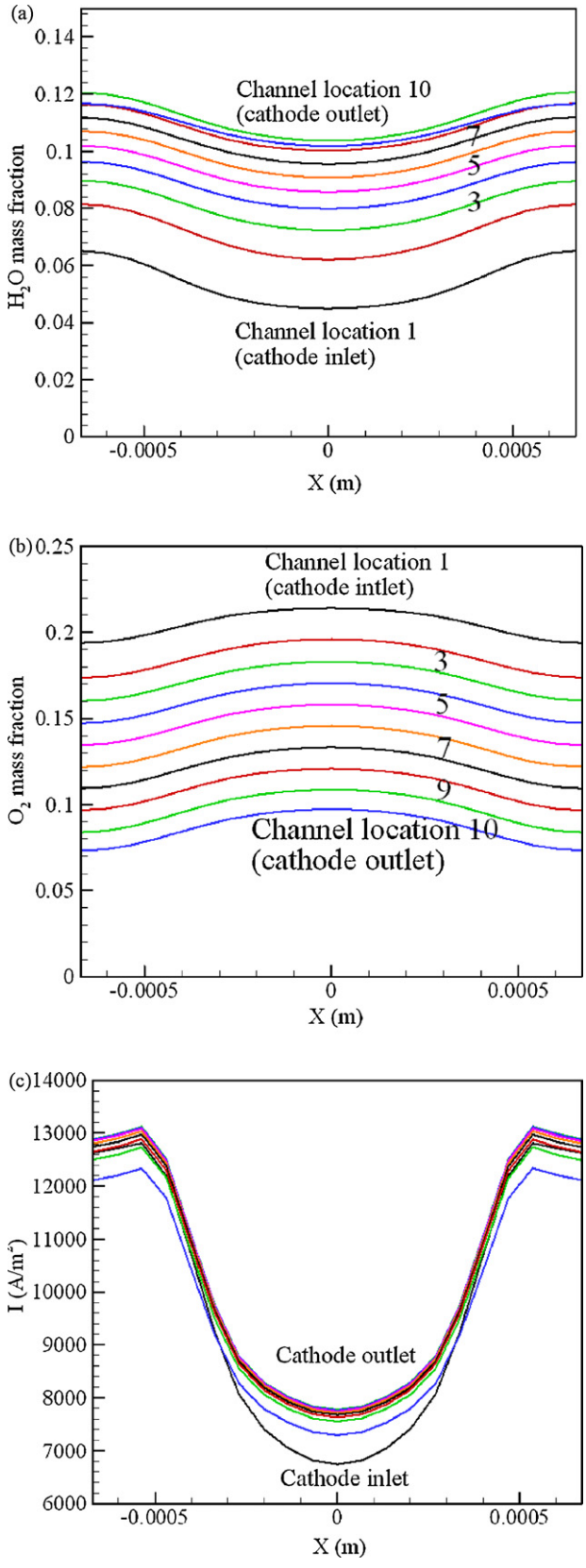

Fig. 10. Profiles at 10 axial locations along the channel: (a) O_2, (b) H_2O and (c) and current density. The numbers in each figure indicate the location from cathode inlet.

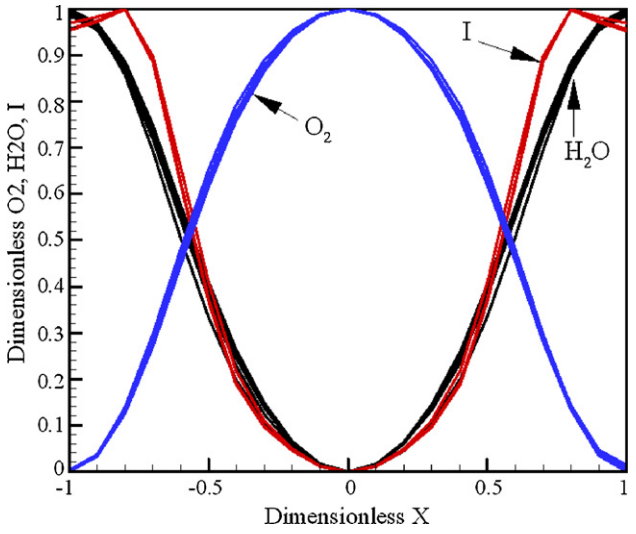

Fig. 11. Normalized profiles for O_2, H_2O mass fraction and current density on GDL/catalyst layer interface.

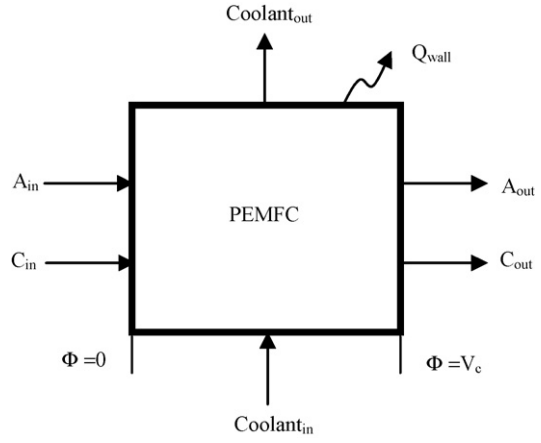

Fig. A1. Illustration of energy balance in a fuel cell.

5. Conclusions

We have presented the modelling framework and development of a comprehensive 3D CFD based simulation code for PEMFC, with a focus on implementation and base case simulations to illustrate the physical features, transport of species along the channel and coupling between heat and mass transfer processes. Analysis of the base case results reveals similarities in the computed cross-sectional profiles along the axial direction of the channels, indicating that dominant coupling of transport phenomena is in the 2D cross-section, This suggest that for unit cells having parallel flow channels, reduced dimensional model based on appropriate similarity variables might provide a useful and fast turnaround alternative to full CFD for initial design and or optimization cycles.

The implementation of a phenomological membrane water transport was shown to yield improved predictions of the global polarization curve. In Part 2 of this work [11] a systematic validation of the CFD code against *spatially* resolved experimental data, including water mass balances and current distribution, is presented together with sensitivity and parametric analyses to fully assess the reliability of the computational tool.

Acknowledgements

Funding for this work was provided to ND by the MITACS Network of Centres of Excellence and Ballard Power Systems. The authors wish to acknowledge the insightful inputs of Jason Chisham, Ryan Mackie, Radu Bradean and John Kenna throughout this work. The authors are also grateful for the support of ESI-CFD through the technical assistance of Ning Zhou and the provision of CFD ACE+ software licenses.

Appendix A. Energy conservation in a PEMFC unit cell

The energy equation can be written as:

$$\nabla(\varepsilon\rho\vec{u}h) = \nabla(-\lambda\nabla T) - \nabla\left(\sum_{i=1}^{N}\vec{J}_i g_i\right) \tag{A1}$$

where the Gibbs free energy can be expressed for each species (charged and neutral) in terms of enthalpy and product of temperature and entropy to become:

$$\nabla(\varepsilon\rho\vec{u}h)=\nabla(-\lambda\nabla T)-\nabla\left(\sum_{\text{neutral}}(\vec{J}_i(h_i-Ts_i))+\sum_{\text{charged}}(\vec{i}_i\phi_i)\right) \tag{A2}$$

The enthalpy in (A2) consists of the enthalpy of formation and sensible heat:

$$h_i = \Delta h^0_{\mathrm{f},i} + \int_{T_0}^{T} Cp\,\mathrm{d}T = \Delta h^0_{\mathrm{f},i} + \tilde{h}_i \tag{A3}$$

Substituting (A3) into (A2) we have

$$\nabla\left(\varepsilon\rho\vec{u}\sum_i(\Delta h^0_{\mathrm{f},i}+\tilde{h}_i)\right) = \nabla(-\lambda\nabla T) - \nabla\left(\sum_{i=1}^{N}\vec{J}_i(\Delta h^0_{\mathrm{f},i}+\tilde{h}_i - Ts_i) + \sum_{\text{charged}}(\vec{i}_i\phi_i)\right) \tag{A4}$$

The species equation from (A4) in Table 1 can be written as

$$\nabla(\varepsilon\rho\vec{V}Y_i) + \nabla\vec{J}_i = \dot{m}_i \tag{A5}$$

Multiplying the enthalpy of formation of each species to (A5), we have

$$\Delta h^0_{\mathrm{f},i}\nabla(\varepsilon\rho\vec{V}Y_i) + \Delta h^0_{\mathrm{f},i}\nabla(\vec{J}_i) = \dot{m}_i\Delta h^0_{\mathrm{f},i} \tag{A6}$$

Summing (A6) for all gas species, we have

$$\nabla(\varepsilon\rho\vec{V}\sum\Delta h^0_{\mathrm{f},i}) + \nabla(\vec{J}_i\sum\Delta h^0_{\mathrm{f},i}) = \sum_{\text{neutral}}\dot{m}_i\Delta h^0_{\mathrm{f},i} \tag{A7}$$

Subtracting (A7) from (A4), we have

$$\nabla\left(\varepsilon\rho\vec{u}\sum_i(\tilde{h}_i)\right) = \nabla(-\lambda\nabla T) - \nabla\left(\sum_{i=1}^{N}\vec{J}_i(\tilde{h}_i - Ts_i) + \sum_{\text{charged}}(\vec{i}_i\phi_i)\right) \quad \text{(A8)}$$

Expanding the electrical potential term in (A8), we have

$$\nabla\left(\sum_{\text{charged}}(\vec{i}_i\phi_i)\right) = (i\nabla\phi + \phi\nabla i)_{\text{H}^+} + (i\nabla\phi + \phi\nabla i)_{\text{e}^-} = \frac{\left|\vec{i}\vec{i}\right|}{\sigma} + (\nabla i)\eta \quad \text{(A9)}$$

With $\nabla i = j_{\text{T}}$, we have

$$\varepsilon C_{\text{p}}\rho\vec{u}\nabla(T) + \nabla(\lambda\nabla T) + \sum_i J_i c_{\text{p},i}\nabla T = \left[j_{\text{T}}\eta + \sum_{i=1}^{N}\vec{j}_i(T\Delta s_i)\right]\left(\frac{S}{V}\right)_{\text{eff}} + \frac{\left|\vec{i}\vec{i}\right|}{\sigma} \quad \text{(A10)}$$

Because liquid water is treated as independently as a different "*species*", the energy due to phase change appears as a source term in (A10). Including the source term for phase change and adding any possible external heat sources, we have the conservation of energy in terms of sensible heat as:

$$\varepsilon C_{\text{p}}\rho\vec{u}\nabla(T) + \nabla(\lambda\nabla T) + \sum_i J_i c_{\text{p},i}\nabla T = \left[j_{\text{T}}\eta + \sum_{i=1}^{N}\vec{j}_i(T\Delta s_i)\right]\left(\frac{S}{V}\right)_{\text{eff}} + \frac{\left|\vec{i}\vec{i}\right|}{\sigma} + \dot{S}_{\text{h}} + \dot{Q} \quad \text{(A11)}$$

The electrical energy that comes out of the system can be calculated using the first law of thermodynamics:

$$\sum_{\text{in}}^{\text{out}}(\dot{m}_i h_i)_{\text{A}} + \sum_{\text{in}}^{\text{out}}(\dot{m}_i h_i)_{\text{C}} + (\dot{m}Cp\Delta T)_{\text{coolant}} = IV_{\text{c}} + \dot{Q}_{\text{wall}} \quad \text{(A12)}$$

$$V_{\text{c}} = \frac{\sum_{\text{in}}^{\text{out}}(\dot{m}_i h_i)_{\text{A}} + \sum_{\text{in}}^{\text{out}}(\dot{m}_i h_i)_{\text{C}} + (\dot{m}Cp\Delta T)_{\text{coolant}} - \dot{Q}_{\text{wall}}}{I} \quad \text{(A13)}$$

Fig. A1 illustrates the relationship among the inlet/outlet of the system and heat/work in a PEMFC system.

Appendix B. Properties of the Springer–Zawodzinski–Gottesfeld membrane model

Water content in the electrolyte phase is related to water activity:

$$\lambda = 0.043 + 17.81a - 39.85a^2 + 36a^3 \quad \text{(B1)}$$

For the vapor phase on the membrane surface the water activity is equal to the relative humidity. The drag coefficient is expressed as a linear function of water content:

$$n_{\text{d}} = \frac{2.5}{22}\lambda \quad \text{(B2)}$$

The diffusion coefficient given by Springer et al. is written as

$$D_{\text{w}} = \frac{\lambda}{(1+s\lambda)^2 a}\frac{\text{d}a}{\text{d}c_{\text{w}}}D' \quad \text{(B3)}$$

where $s = 0.126$ is the swelling factor and D' is fitted piecewise as

$$\begin{aligned} D' &= 0.25\lambda, \quad 0 < \lambda \le 2 \\ D' &= 0.5 + 0.8125(\lambda - 2), \quad 2 < \lambda \le 6 \\ D' &= 3.75 + 0.267(\lambda - 6), \quad 6 < \lambda \end{aligned} \quad \text{(B4)}$$

The protonic conductivity of the electrolyte is given by

$$\sigma = (0.005139\lambda - 0.00326)\exp\left(1268\left(\frac{1}{303}\right) - \left(\frac{1}{T}\right)\right) \quad \text{(B5)}$$

Membrane density $\rho_{\text{m}} = 2000\,\text{kg m}^{-3}$ and equivalent weight $M_{\text{w}} = 1.1\,\text{kg mol}^{-1}$ are used in the calculation.

References

[1] V. Gurau, H.T. Liu, S. Kakac, AIChE J. 44 (11) (1998) 2410–2422.
[2] S. Um, C.Y. Wang, K.S. Chen, J. Electrochem. Soc. 147 (12) (2000) 4485–4493.
[3] S. Dutta, S. Shimpalee, J.W. Van Zee, Int. J. Heat Mass Transf. 44 (11) (2001) 2029–2042.
[4] T. Berning, N. Djilali, J. Electrochem. Soc. 150 (12) (2003) A1589–A1598.
[5] S. Mazumder, J.V. Cole, J. Electrochem. Soc. 150 (11) (2003) A1503–A1509.
[6] S. Mazumder, J.V. Cole, J. Electrochem. Soc. 150 (11) (2003) A1510–A1517.
[7] T.H. Zhou, H.T. Liu, J. Power Sources 138 (1/2) (2004) 101–110.
[8] S. Li, U. Becker, A three dimensional CFD model for PEMFC. ASME Fuel Cell Science, in: 2nd Engineering and Technology Conference, Rochester, NY, 2004.
[9] S. Li, J. Cao, W. Wangard, U. Becker, Modeling PEMFC with Fluent. ASME Fuel Cell Science, in: 3rd Engineering and Technology Conference, Ypsilanti, MI, 2005.
[10] N. Djilali, Energy 32 (4) (2007) 269–280.
[11] P.C. Sui, S. Kumar, N. Djilali, J. Power Sources 180 (2008) 423–432.
[12] P.C. Sui, N. Djilali, J. Fuel Cell Sci. Technol. 2 (2005) 149–155.
[13] S. Mazumder, J. Electrochem. Soc. 152 (8) (2005) A1633–A1644.
[14] T.E. Springer, T.A. Zawodzinski, S. Gottesfeld, J. Electrochem. Soc. 138 (8) (1991) 2334–2342.
[15] G.J.M. Janssen, J. Electrochem. Soc. 148 (12) (2001) A1313–A1323.
[16] J. Fimrite, H. Struchtrup, N. Djilali, J. Electrochem. Soc. 152 (9) (2005) A1804–A1814.
[17] J.H. Nam, M. Kaviany, Int. J. Heat Mass Transf. 46 (24) (2003) 4595–4611.

[18] W.K. Lee, J.W. Van Zee, A. Jena, K. Gupta, Fuel Cell Seminar, Palm Springs, 2004.
[19] W. Sun, B.A. Peppley, K. Karan, J. Power Sources 144 (1) (2005) 42–53.
[20] E.A. Ticianelli, C.R. Derouin, A. Redondo, S. Srinivasan, J. Electrochem. Soc. 135 (9) (1988) 2209–2214.
[21] CFD-ACE+ User's Manual, ESI-CFD, Huntsville, AL, 2006.
[22] S.A. Freunberger, M. Reum, J. Evertz, A. Wokaun, F.N. Buchi, J. Electrochem. Soc. 153 (11) (2006) A2158–A2165.
[23] J.S. Yi, T.V. Nguyen, J. Electrochem. Soc. 145 (4) (1998) 1149–1159.
[24] P. Berg, K. Promislow, J. St Pierre, J. Stumper, B. Wetton, J. Electrochem. Soc. 151 (3) (2004) A341–A353.
[25] Unpublished experimental data, Ballard Power System, 2007.